Renewable Energy 200 (2022) 809–820

Contents lists available at ScienceDirect

Renewable Energy

journal homepage: www.elsevier.com/locate/renene

Concentration performance of solar collector integrated compound parabolic concentrator and flat microchannel tube with tracking system

Rongji Xu [a,*], Zhencheng He [a], Liwei Yang [b], Shuhui Xu [a], Ruixiang Wang [a], Huasheng Wang [b]

[a] Beijing Engineering Research Center of Sustainable Energy and Buildings, Beijing University of Civil Engineering and Architecture, Beijing, 100044, China
[b] School of Material Science and Engineering, Queen Mary University of London, London, E1 4NS, UK

ARTICLE INFO

Keywords:
Solar collector
Compound parabolic concentrator
Microchannel tube
Tracking
Heat flux
Rotation angle

ABSTRACT

The compound parabolic concentrator is a non-imaging concentrator that can concentrate solar radiation without tracking system. However, as the concentration ratio increases, the maximum half acceptance angle and the effective working hours decrease. To increase the effective working hours at high concentration ratio, a tracking solar collector is proposed that integrates the compound parabolic concentrator and flat microchannel tube. This new solar collector can track solar radiation by rotating the two reflective surfaces around their respective starting lines. A two-dimensional model is developed for the irradiation concentration of the tracking compound parabolic concentrator. For the geometry of the compound parabolic concentrator and solar irradiant angle, the optimal rotation angles of the reflective surfaces are determined to minimize the irradiation loss. The effects of the rotation angle of the two reflective surfaces on the concentration performance are simulated. The simulation results show that in the tracking mode, the averaged heat flux on the surface of the absorber can reach 7.61 kW m^{-2} when the concentration ratio and truncation ratio are 8 and 0.5, respectively. Even when the incident angle of solar irradiation is 30°, the averaged heat flux is still 5.12 kW m^{-2}. Compared with other kinds of reflector, the concentration performance of the compound parabolic concentrator is merely influenced by the tracking error. The positive and negative tracking errors lead to different declining rates of normalized optical efficiency and the influence of positive tracking error is more acceptable.

1. Introduction

Among kinds of clean energy, solar energy is universal and free. Solar thermal system [1] is an attractive approach to make use of solar energy. Compound parabolic concentrator (CPC) is a kind of non-imaging concentrator that can concentrate solar irradiation without tracking device. CPC has great application potential to collect solar thermal energy at low temperature (100–200 °C) due to its large acceptance angle [2]. CPC was first proposed by Winston [3] for solar thermal energy collection. Up to now, CPC has been developed and widely used in photo-thermal [4] and photovoltaic [5] systems with good concentration performance.

Current studies are mainly focused on CPC with low concentration ratio (<4) [6], which has a large maximum half acceptance angle (HAA_{max}), and can work for long time without tracking. However, in this case, the energy density obtained is low and sometimes cannot achieve the required collection temperature or collector efficiency. Tang et al. [7] proposed a method to estimate the annual energy collected. For the east-west oriented solar collector, the HAA_{max} that can maximize the annual energy collected is between 25.3° and 26° in China, the maximum annually averaged concentration ratio is 1.45–1.74.

Increasing the concentration ratio inevitably reduces the HAA_{max} and reduces the effective working hours of CPC. To avoid this problem, solar tracking system is used for CPC. Chen et al. [8] established a mathematical model to calculate the effect of seasonal adjustment for a CPC placed in east-west direction, and determined the best inclination angle in different seasons. Wang et al. [9] proposed a single-axis tracking CPC vacuum tube heat pipe collector that can rotate around the collector axis to track the position of the sun. The experimental results showed that the collector efficiency was much higher than that of the non-tracking collector. Waghmare et al. [10] designed a CPC collector with five tracking modes and analyzed the tracking effect for each mode. The numerical results suggested that when the collector is placed in east-west direction and continuously tracking, the heat flux is higher and the tracking frequency is lower. This is superior to a parabolic trough collector (PTC) with nearly the same aperture area when the

* Corresponding author.
E-mail address: xurongji@bucea.edu.cn (R. Xu).

https://doi.org/10.1016/j.renene.2022.09.107
Received 17 August 2022; Received in revised form 12 September 2022; Accepted 24 September 2022
Available online 30 September 2022

tracking frequency is designed to be 2.33 per day. Achkari et al. [11] proposed a solar tracking scheme based on continuous testing to increase the net energy collected by tracking. The study found that biaxial tracking can obtain the maximum amount of energy collected. East-west tracking is more effective at high latitude and altitude. Yazdanbakhsh et al. [12] found that CPC with solar tracking system can improve the photo-thermal conversion efficiency by 2–3 times when using CPC for photodegradation of organic compounds.

However, the problem is that the radiation reaching the absorber is non-uniform after reflection [13,14], which reduces service life of the coating on the absorber surface due to the large temperature difference, and even damages the absorber. For the CPC with tube absorber, Xu et al. [15] used Monte Carlo ray tracing (MCRT) method to analyze the influence of CPC deformation on the concentration performance. The results suggest that small inner rotation, small inner and outer translations of reflection surface and truncation of involute starting point can impact the heat flux distribution on the absorber. Xu et al. [16] proposed a multi-sectioned CPC based on genetic algorithm, which can significantly reduce the inhomogeneity of heat flux distribution on the surface of the receiver. The averaged energy heterogeneity coefficient of M-CPC can be reduced from 2.23 to 0.92 by using five reflective planes on the single side. For flat-plate CPC collectors, the uneven distribution of heat flux on the absorber also exists. Microchannel flat tube [17] with high thermal conductivity [18,19] can be used as absorber of CPC collector to reduce the temperature difference caused by non-uniformly heat flux. Wang et al. [20] proposed a BIPV/T system based on microchannel flat heat pipe. Due to the decrease of thermal resistance and increase of heat exchange area of the system, the maximum averaged total efficiency of the system reached 50.4%.

Although adding a tracking system to the collector can prolong the effective heat collection time of the system and greatly increase the energy collected. However, the aforementioned tracking CPC often requires a large tracking system and hence is difficult to match the building structure. In addition, a large amount of power is consumed during tracking, reducing the benefits brought by the tracking system. In the present study, a tracking CPC-microchannel tube solar collector (TCPCMSC) is proposed. Different from the conventional tracking method, the absorber and collector frame are fixed, and the two reflective surfaces of CPC are independently controlled by uniaxial tracking according to solar irradiation angle. The tracking system is integrated inside the collector, which is almost unaffected by the external environment and has good reliability. The optimal rotation angle (ORA) of CPC is determined for tracking control. Based on a two-dimensional CPC irradiation tracing model, the influence of CPC rotation angle on concentration performance is studied.

2. Design of tracking CPC-microchannel tube solar collector

In this section, the components of TCPCMSC and the sun tracking mode are described in detail.

2.1. Two-dimensional structure of the CPC

As shown in Fig. 1, the CPC consists of two symmetric parabolic segments. The reflective surfaces are defined by Eq. (1) [21]:

$$y=\frac{x^2}{2s(1+\sin\theta_{max})} \tag{1}$$

Where s is the width of the microchannel absorber; θ_{max} is the maximum half acceptance angle of CPC.

The coordinates of the starting point are defined by Eqs. (2) and (3):

$$x_s=s\cos\theta_{max} \tag{2}$$

$$y_s=\frac{s}{2}(1-\sin\theta_{max}) \tag{3}$$

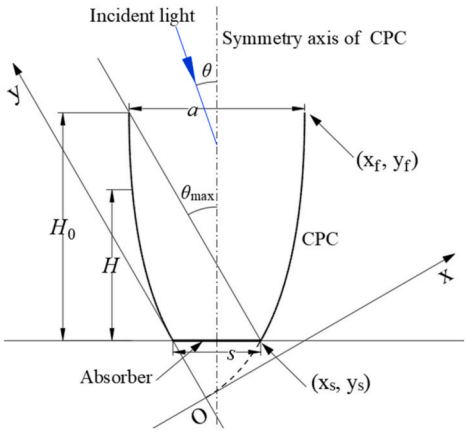

Fig. 1. 2D schematic of CPC.

The coordinates of the end point are defined by Eqs. (4) and (5):

$$x_f=(s+a)\cos\theta_{max} \tag{4}$$

$$y_f=\frac{s}{2}(1-\sin\theta_{max})\left(1+\frac{1}{\sin\theta_{max}}\right)^2 \tag{5}$$

Where a is the aperture of CPC.

The concentration ratio of CPC is defined by Eq. (6):

$$C=\frac{1}{\sin\theta_{max}} \tag{6}$$

The height of CPC, H_0, is the vertical distance from the aperture to the starting point. The truncated height, H, is the vertical distance from the truncated aperture to the starting point. The truncation ratio C_t is defined by Eq. (7):

$$C_t=\frac{H}{H_0} \tag{7}$$

The solar incidence angle, θ, is defined as the angle between the solar irradiation and the symmetry axis of CPC (see Fig. 1). The incidence angle is positive when the solar irradiation enters from the left side of the symmetry axis, and negative when the solar irradiation enters from the right side of the symmetry axis.

2.2. Structure of the tracking CPC-microchannel tube solar collector and its working mode

As shown in Fig. 2, the structure of TCPCMSC includes tracking CPC, microchannel tube absorber, glass cover plate, frame, insulation layer, inlet header and outlet header. A CPC and microchannel tube absorber form a collection unit. To avoid mutual influence of tracking rotation or occlusion of the sunlight, gaps are left between multiple parallel collection units for tracking rotation. TCPCMSC is south-faced with CPC in east-west direction. The collector is fixed and solar tracking is achieved only by the rotational motion of the reflective surfaces. The starting lines for the reflective surfaces of a CPC are taken as the rotation axes, respectively. The rotation is continuous according to the changes of the solar elevation angle over time. In this way, even if the solar incidence angle is larger than the HAA_{max}, the solar irradiation can still be concentrated to the absorber surface. When the solar incidence angle is smaller than the HAA_{max}, the reflective surfaces are expanded to enlarge the width of the aperture to allow more solar irradiation entering the CPC and to increase the concentration ratio. Compared with the fixed CPC, though there are gaps between the collection units, the thermal energy absorbed by the absorber can be increased no matter whether the solar incidence angle is smaller or larger than the HAA_{max}.

When the solar incidence is not perpendicular to the CPC aperture,

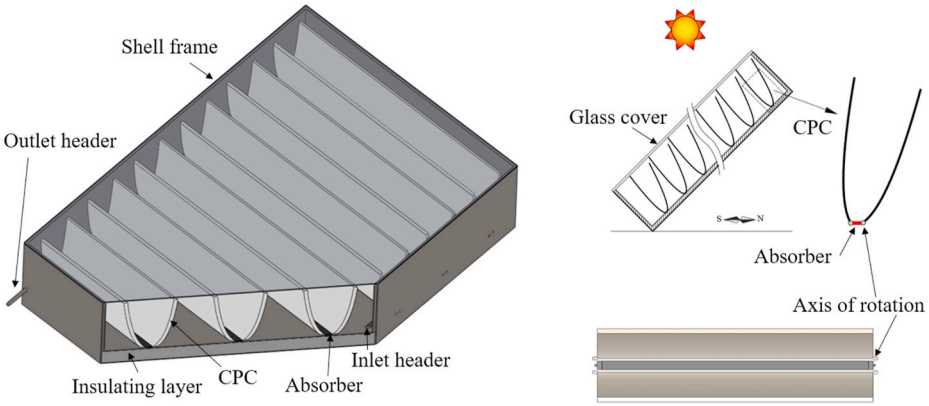

Fig. 2. Schematic of TCPCMSC

the concentrating effects of the left reflective surface (CPC-L) and right reflective surface (CPC-R) are different. Therefore, the rotation tracking rules of the two reflective surfaces are different and independent of each other. Since the two reflective surfaces of CPC are symmetric, the positive and negative solar incidence. In this study, as an example, the positive solar incidence is selected.

The two rotation tracking rules for CPC-R include the counterclockwise rotation when the solar incidence angle is larger than the HAAmax and the clockwise rotation when the solar incidence angle is smaller than the HAAmax. As shown in Fig. 3, when the incident angle is larger than the HAAmax, without rotation tracking, the incidence reflected by CPC-R (blue dotted line) cannot reach the surface of the absorber, but reflects to CPC-L and finally escapes from CPC. In this case, the counterclockwise rotation of CPC-R can concentrate the incidence (solid blue line) on the surface of the absorber. The ORA is defined as the rotation angle where the incidence reflected by the end point of the rotated CPC-R can reach the left end of the absorber. When the incident angle is smaller than the HAAmax, as shown in Fig. 3(b), without rotation tracking, the reflected incidence can reach the absorber, but cannot cover the whole surface of the absorber, resulting in uneven distribution of heat flux on the absorber. In this case, clockwise rotation can make the incidence cover the entire surface of the absorber after reflection, which increases the width of the CPC aperture, the amount of incidence and the uniformity of the heat flux distribution, and avoids the energy loss caused by the gaps between the collection units. The ORA is defined as the rotation angle where the incidence reflected from the starting point of the rotated CPC-R can reach the left end of the absorber.

The two rotation tracking rules for CPC-L include counterclockwise rotation for large incident angle where the CPC-L cannot concentrate the incidence, and small incident angle where the CPC-L can concentrate incidence. When the incident angle is large, as shown in Fig. 4(a), CPC-L

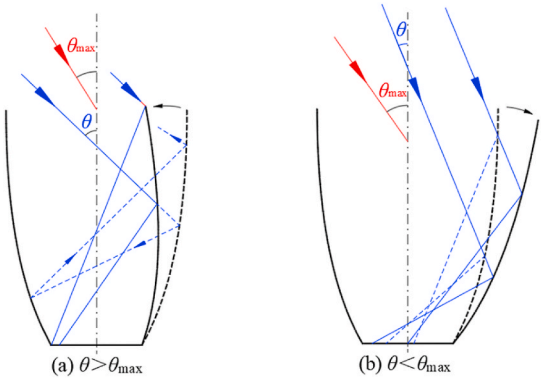

Fig. 3. Schematic for the influence of CPC-R rotation on concentration performance.

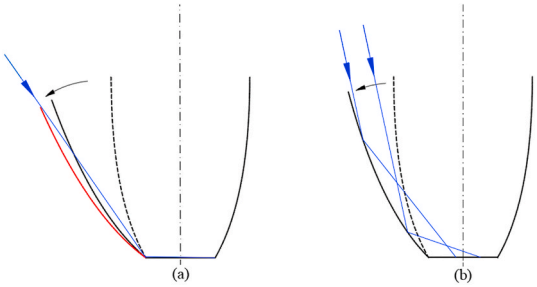

Fig. 4. Schematic for the influence of CPC-L rotation on concentration performance.

cannot concentrate the incidence due to its own occlusion. To make full use of the gap caused by the rotation of adjacent CPCs, the amount of incidence entering the CPC should be increased as much as possible. In this case, the ORA is defined as the angle where the line connecting the starting point and ending point is parallel to the incidence. When the incident angle is small, as shown in Fig. 4(b), CPC-L can concentrate the incidence to absorber. The ORA is defined as the rotation angle where the incidence reflected from the starting point of rotated CPC-L can reach the right end of the absorber.

3. Derivation and calculation for optimal rotation angle

As shown in Fig. 5, the incidence angle, θ, can be obtained according to the inclination angle of the collector, β, and the solar elevation angle, α (determined by latitude φ, days n and time T). The rotation angle δ corresponding to the incident angle θ is defined to be positive for counterclockwise rotation and negative for clockwise rotation. Therefore, the rotation angle for any latitude (on northern hemisphere) and

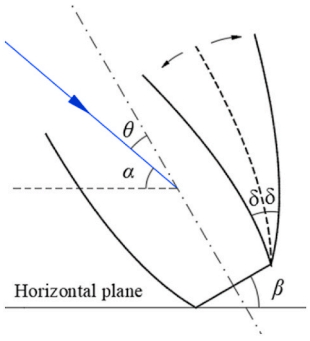

Fig. 5. Schematic for the incident angle and the rotation angle.

any time can be expressed as$\delta = f(\beta, T, n, \varphi)$, where δ is a function of collector inclination angle, position and time.

3.1. Solar incidence angle

The solar incidence angle is expressed by Eq. (8):

$$\theta = |\alpha + \beta - 90^{\circ}| \tag{8}$$

Where β is the inclination angle of TCPCMSC; α is the solar elevation angle, as defined by Eq. (9):

$$\sin\alpha = \sin\varphi \sin\sigma + \cos\varphi \cos\sigma \cos\omega \tag{9}$$

Where φ is the latitude of the position; σ is the sun declination angle, expressed by Eq. (10):

$$\sigma = 23.45 \sin\left(360^{\circ} \times \frac{284 + n}{365}\right) \tag{10}$$

The solar hour angle, ω, is defined by Eq. (11):

$$\omega = 15 \times T - 180 \tag{11}$$

3.2. Derivation and calculation of the optimal rotation angle of CPC-R

As shown in Fig. 6(a), when the incident angle is larger than the HAA_{max}, the CPC-R rotates counterclockwise around the starting point O from OR to OR'. The relationship between the incident angle and the ORA can be expressed by Eq. (12) (see Appendix I for the derivation details):

$$\theta = \arctan\left(\frac{s + \frac{H}{\sin\varepsilon}\cdot\cos\left(\varepsilon + \delta_{R,ORA}\right)}{\frac{H}{\sin\varepsilon}\cdot\sin\left(\varepsilon + \delta_{R,ORA}\right)}\right) + 2\lambda' \tag{12}$$

Where λ' is the angle between the tangent line of CPC at point R′ and the vertical direction; ε is the angle between OR and the absorber.

When the incident angle is smaller than the HAA_{max}, as shown in Fig. 6(b). CPC-R rotates clockwise around the starting point O. The rotation angle is the angle between the tangent lines of CPC-R at starting points before and after the rotation. The ORA is the rotation angle where the incidence can reach point P after reflected from point O. The ORA is determined by Eq. (13) (see Appendix II for the derivation details):

$$\delta_{R,ORA} = \eta - \frac{90^{\circ} + \theta}{2} \tag{13}$$

3.3. Derivation and calculation of the optimal rotation angle of CPC-L

As shown in Fig. 7, when incidence enters the CPC from the left side, CPC-L rotates counterclockwise around the starting point P. The ORA are determined by Eq. (14) (see Appendix III for the derivation details):

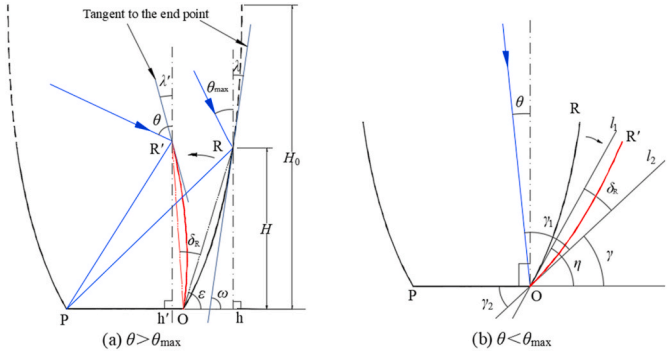

Fig. 6. Schemetic for the optimal rotation angle of CPC-R.

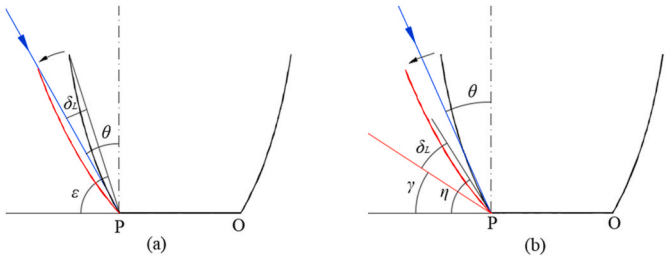

Fig. 7. Schemetic for the optimal rotation angle of CPC-L.

$$\delta_{L,ORA} = \max\begin{cases} \eta - \dfrac{90^{\circ} - \theta}{2} \\ \varepsilon + \theta - 90^{\circ} \end{cases} \tag{14}$$

4. Simulation of concentration performance of tracking CPC-microchannel tube solar collector

A two-dimensional ray tracing model was established using COMSOL-Multiphysics software. According to the heat flux distribution on the absorber surface, the concentrating performance of TCPCMSC is analyzed.

4.1. Physical model

A two-dimensional numerical model of CPC was established according to the two-dimensional geometry of CPC. The width of the model's absorber was fixed at 0.02 m and the CPC truncation residual ratio was 0.5 [22,23].

4.2. Model validation

The model is validated by the experimental data of Smyth et al. [24]. For the purpose of comparison, the conditions in the experiments are used for simulations of this model: the width of the absorber is set to be 0.2 m, the concentration ratio of the CPC is 1.6, the truncation residual ratio of the CPC is 0.5, the reflectivity of CPC surfaces is 0.8, and the incident angle is 0°. Fig. 8 shows the comparison between the heat flux distribution predicted by this model, the experimental data and simulation results of Smyth et al. [24]. The simulation results by this model

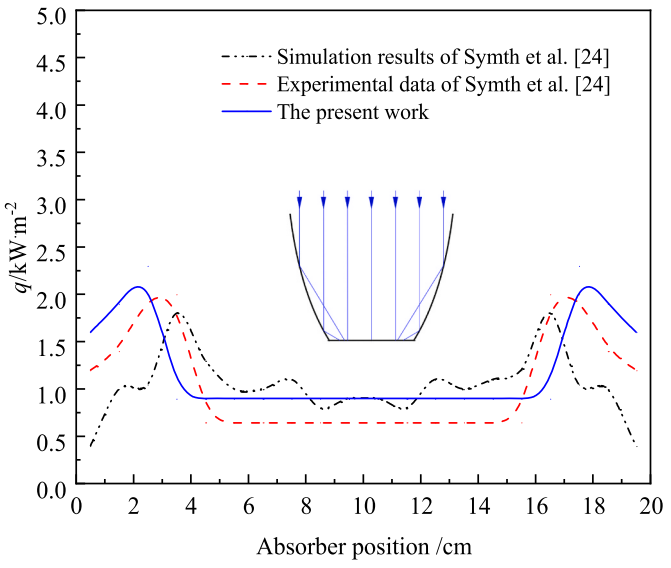

Fig. 8. Comparison of heat flux distribution between Smyth's results and the present work.

are found to be in good agreement with the experimental data and simulation results of Smyth et al. [24].

4.3. Working conditions of the numerical simulation

The concentration performance of the CPC under different incident angles is firstly simulated without any rotation. Then the reflection performance of the CPC-R under different incident angles and rotation angles is studied with the CPC-L at rest. Similarly, the reflection performance of the CPC-L under different incident angles and rotation angles is studied with the CPC-R at rest. Fourthly, when both reflection surfaces of the CPC are under the ORA, the concentration performance of tracking CPC under different incident angles is analyzed. Finally, the influence of the tracking error on concentration performance of the CPC is analyzed according to the variation of concentration performance as the rotation angle deviated from the ORA. The working conditions of the numerical simulations are summarized in Table 1.

5. Results and discussion

The cases listed in section 3.3 are simulated and the simulation results are obtained. The effects of different conditions on the concentration performance of TCPCMSC are analyzed.

5.1. Influence of the incident angle on concentration performance of non-tracking CPC

Fig. 9 shows the influence of the incident angle on the heat flux distribution on the absorber surface when the concentration ratio of the CPC is 8 without tracking. When the incident angle is 0° (as shown in Fig. 10(a)), the heat flux on absorber surface is symmetrically distributed. From the edge to the center of the absorber surface, there are three peaks of heat flux, increasing successively. With the increase of the incident angle, the heat flux distribution is deflected to the direction of incidence deflection. The magnitude of the first peak of heat flux on the deviating side decreases and the second and third peaks disappear. This may be explained as: as shown in Fig. 10(b and c), as the incident angle increases, more incidence is reflected by CPC-R and concentrated on the absorber surface, while the incidence reflected by CPC-L decreases. When the incident angle is close to the HAA_{max} ($\theta = 7.18°$), the peak of heat flux on the deviating side reduces and that on the other side increases. Overall, the averaged heat flux does not change significantly.

When the incident angle is larger than the HAA_{max} (as shown in Fig. 10(d and e)), most of the reflected incidence cannot reach the absorber surface. The heat flux on the absorber surface decreases sharply, even to zero in some areas ($\theta = 10°$). In this case, only when the incident angle is smaller than the HAA_{max} can the absorber surface obtain a high heat flux. For the CPC with a concentration ratio of 8, e.g., the HAA_{max} is 7.18° and the corresponding effective working hours is only 0.96 h. To increase the total solar thermal energy collected over a day, the CPC with a high concentration ratio is essential to order to extend the effective working hours.

Table 1
Working conditions of the numerical simulation.

Cases	Introduction	C	C_t	θ, °	δ_L, °	δ_R, °
1	The influence of the incident angle on concentration performances	8	0.5	0/4/6/8/10	0	0
2–1	Effect of CPC-R rotation on concentration performances ($\theta > \theta_{max}$)	8	0.5	37	27	26/28/30/32/34
2–2	Effect of CPC-R rotation on concentration performances ($\theta < \theta_{max}$)	8	0.5	0	−9.9	0/-2/-4/-6/-8
3	Effect of CPC-L rotation on concentration performances	8	0.5	10	4.7/6.7/8.7/10.7/12.7	20
4	Concentration performances of tracking CPC at ORA	6/8/10	0.5	0–40	$\delta_{L,ORA}$	$\delta_{R,ORA}$
5	Influence of tracking error on CPC concentration performances	6/8/10	0.5	35	$\delta_{L,ORA}$	23–33

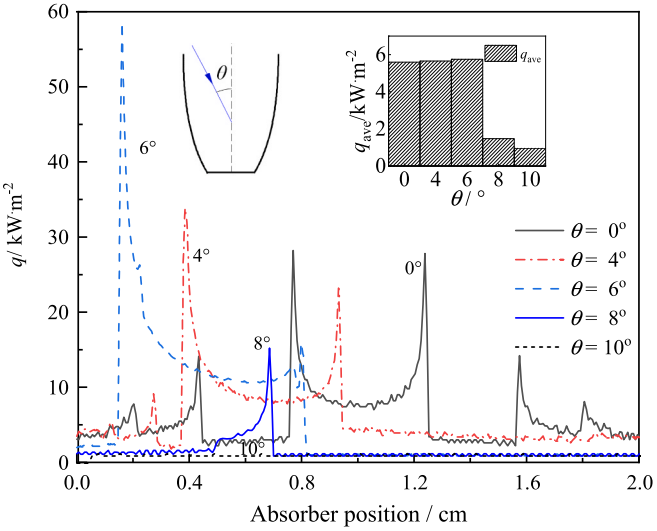

Fig. 9. Effect of the incident angle on heat flux distribution on the absorber surface without tracking
($C = 8, \delta = 0°$)

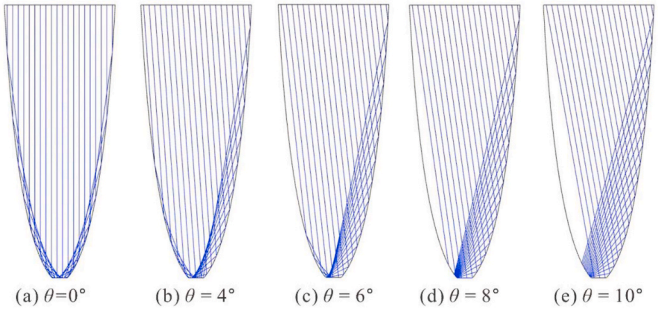

Fig. 10. Schematics of ray tracing at different incidence angles ($C = 8$, $\delta = 0°$).

5.2. Effect of CPC-R rotation on concentration performance

The simulations for the tracking modes of CPC-R under incident angles larger and smaller than the HAA_{max} are different, as well as the concentration performance. To avoid the influence of CPC-L on the results, the CPC-L is rotated to a position where the CPC-L cannot work. The lines connecting the starting and ending points of CPC-L are parallel to the incidence, as shown in Fig. 11.

When the incident angle ($\theta = 37°$) is larger than the HAA_{max} ($\theta_{max} = 7.18°$), and the CPC-R rotation angle is approximately the ORA ($\delta_{R,ORA} = 30°$), the heat flux on the absorber surface changes, as shown in Fig. 11. It can be seen that even though the incidence is much larger than the HAA_{max}, the CPC-R with rotation tracking can still concentrate the incidence on the absorber. When the CPC-R is rotated by the ORA ($\delta_{R,ORA} = 30°$), the heat flux on the absorber surface decreases gradually from the left side to the right side. The reason is that the left end of the absorber is close to the focus of the CPC-R, which results in the peak heat

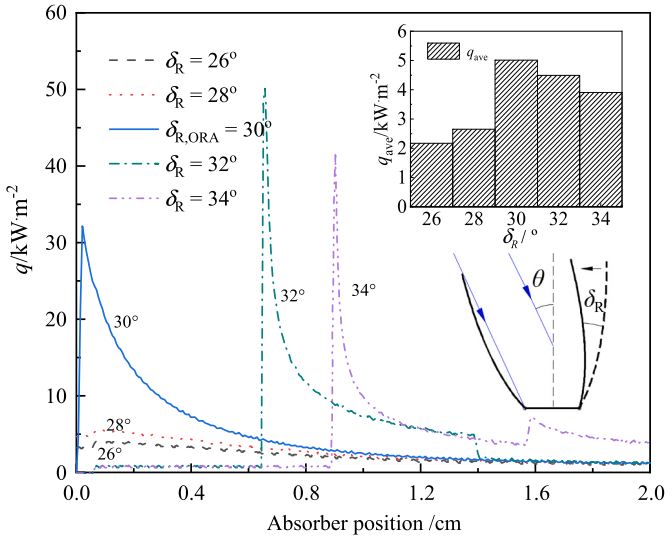

Fig. 11. Effect of rotation angle for CPC-R on heat flux distribution on absorber surface ($C = 8$, $\theta = 37°$)

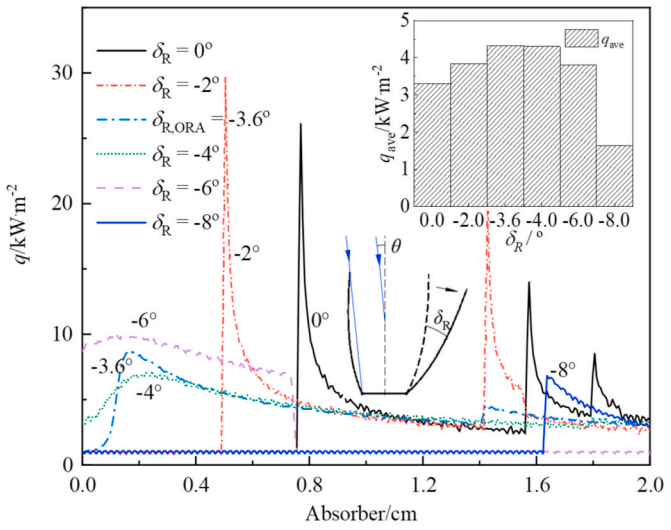

Fig. 13. Effect of rotation angle for CPC-R on heat flux distribution on absorber surface ($C = 8$, $\theta = 0°$).

flux, as shown in Fig. 12(c). The heat flux at the right end of the absorber decreases to about 1 kW m^{-2} and the averaged heat flux on the absorber surface is 5.01 kW m^{-2}. When the rotation angle is smaller than the ORA, the peak of heat flux is not apparent and the averaged heat flux on the absorber surface is low. This is caused by the small rotation angle where a large amount of incidence cannot be reflected to the absorber, as shown in Fig. 12(a and b). When the rotation angle is larger than the ORA, the peak of heat flux moves to right. The heat flux distribution on the left side of the peak is all produced by direct incidence. The heat flux distributes on the right side of the peak is generated by reflected and direct incidences with increase in magnitude. However, as the rotation angle increases further, the CPC aperture becomes smaller (as shown in Fig. 12(d and e)). The incidence decreases and hence the magnitude of the peak heat flux decreases.

When the incident angle ($\theta = 0°$) is smaller than the HAA_{max} ($\theta_{max} = 7.18°$), as the CPC-R rotates clockwise around the starting point by about the ORA, the heat flux on the absorber surface varies as shown in Fig. 13. When the CPC-R is rotated by the ORA ($\delta_{R,ORA} = -3.6°$), the heat flux on the absorber surface distributes evenly. The averaged heat flux is 4.3 kW m^{-2}. A large peak of heat flux occurs near the left end of the absorber. The heat flux on the left side of the peak is the same as the incidence irradiance (about 1 kW m^{-2}) and the much higher heat flux occurs on the right side of the peak. It can be seen from Fig. 14(c) that when the CPC-R is rotated by the ORA, the incidence reaching the absorber surface is relatively evenly distributed. Only a small area on the left side of the absorber receives a little incidence and hence the heat flux is very low. When the rotation angle of CPC-R is larger than the ORA, the heat flux at the left end of the absorber increases. A large area of low heat flux appears on the right side of the absorber and the averaged heat flux decreases. This is because as the rotation angle increases (as shown in

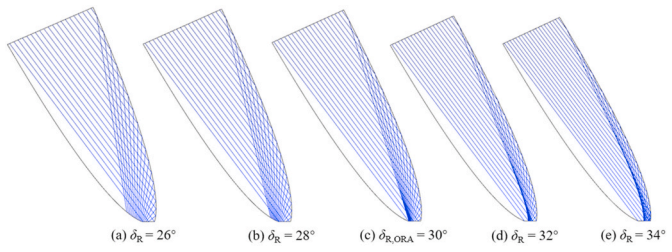

Fig. 12. Schematics of ray tracing at different rotation angles for CPC-R ($C = 8$, $\theta = 37°$).

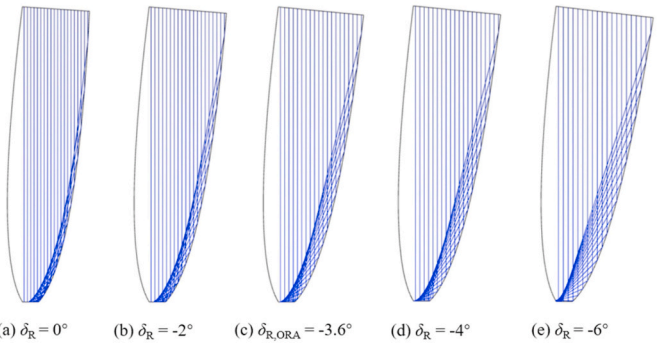

Fig. 14. Schematics of ray tracing under different rotation angles for CPC-R ($C = 8$, $\theta = 0°$).

Fig. 14(d and e)), the peak of heat flux moves to left. Part of the incidence cannot reach the absorber surface. When the rotation angle of CPC-R is smaller than the ORA, there are three peaks of heat flux on the absorber surface, successively decreasing from left side to right side. The magnitude of heat flux in the left side of the first peak is only 1 kW m^{-2}. As seen from Fig. 14(a and b), the incidence rays reflected by CPC-R cannot reach the left end of the absorber. The CPC aperture decreases and hence the magnitude of the averaged heat flux decreases. In this case, when the CPC-R is rotated by the ORA, the maximum value of averaged heat flux on the absorber surface is obtained whereas when the rotation angle is not the ORA, the averaged heat flux is lower.

5.3. *Effect of CPC-L rotation on concentration performance*

To avoid the influence of CPC-R on the results, the CPC-R is rotated to a position where the CPC-R does not work. The lines connecting the starting and ending points of CPC-R are parallel to the incidence. When the incident angle ($\theta = 10°$) is larger than the HAA_{max} ($\theta_{max} = 7.18°$), and the CPC-L rotation angle is approximately the ORA ($\delta_{L,ORA} = 8.7°$), the heat flux on the absorber surface varies, as shown in Fig. 15. When the CPC-L is rotated by the ORA ($\delta_{L,ORA} = 8.7°$), the heat flux on the left side of the absorber surface is relatively high with several peaks. The heat flux distributes evenly at the middle of the absorber surface and decreases to 1 kW m^{-2} on the right side. When the rotation angle is larger than the ORA, the peak heat flux on the left side gradually moves to the right side with an increase in magnitude. The heat flux on the right

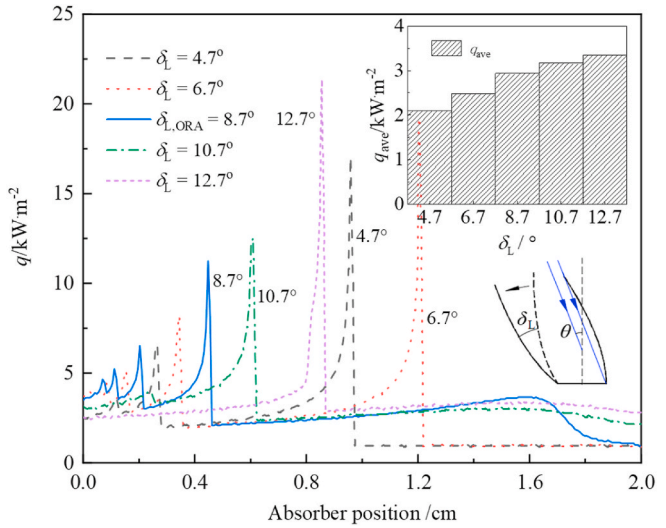

Fig. 15. Effect of rotation angle for CPC-L on heat flux distribution on absorber surface (C = 8, θ = 10°).

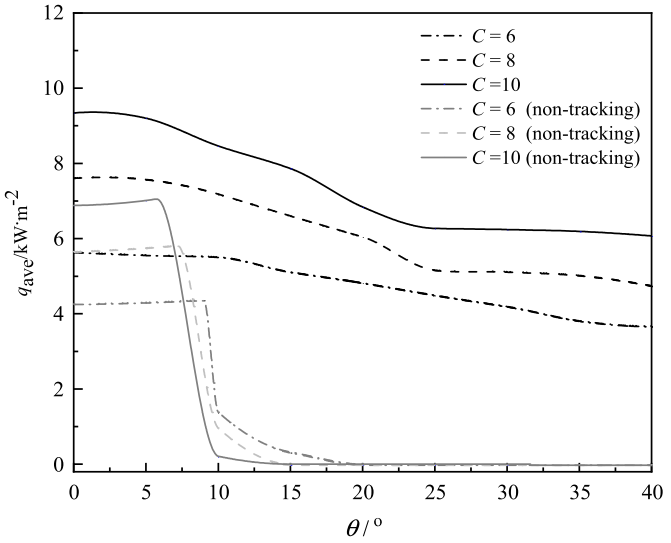

Fig. 17. Heat flux on absorber of TCPCMSC at different incident angles ($\delta_L = \delta_{L,ORA}$, $\delta_R = \delta_{R,ORA}$).

side distributes more uniformly and the averaged heat flux increases. It can be seen from Fig. 16(d and e) that with the increase in rotation angle, a small amount of incidence cannot reach the absorber surface while the increase in CPC aperture and the increase in concentration ratio lead to the increase in averaged heat flux. When the rotation angle is smaller than the ORA, the heat flux with large magnitude mainly distributes on the left side surface, making the heat flux distribution on the absorber surface more uneven. As shown in Fig. 16(a and b), the incidence reflected by CPC-L only reaches the left side of the heat absorber (microchannel tube). The decrease in the CPC aperture also leads to a decrease in the averaged heat flux. For CPC-L, when the rotation angle is larger than the ORA, the averaged heat flux is increased slowly. When the rotation angle is smaller than the ORA, the averaged heat flux decreases. When CPC-L rotates by a rotation angle larger than the ORA, the heat collected is higher. Therefore, situations where the rotation angle is smaller than the ORA should be avoided.

5.4. Concentration performance of tracking CPC at optimal rotation angle

Fig. 17 shows the averaged heat flux on the absorber surface under different incident angles and concentration ratio when both sides of CPC are rotated by the ORA. It can be seen that the averaged heat flux on the absorber surface decreases with the increase of the incident angle at different concentration ratios. However, the slope is different at different concentration ratios. When the concentration ratio is relatively high (C = 8, C = 10), the slope of decrease in heat flux decreases at incidence angle of 25°. This mainly results from the fact that with the increase of the incident angle, to meet the ORA on both sides of CPC, the CPC aperture becomes narrower, the amount of incidence decreases, and the averaged heat flux on the absorber surface decreases. When the incident angle increases further, the CPC-L cannot work. In this case, the ORA is the rotation angle where CPC-L does not hide the absorber. The decreasing rate of CPC aperture decreases. Therefore, the slope of decrease in averaged heat flux decreases. When the concentration ratio is relatively low (C = 6), the averaged heat flux decreases almost linearly with the increase of incident angle. However, the averaged heat flux on the absorber surface can reach 3.94 kW m^{-2} even when the incident angle is 40°.

When the incident angle is relatively small, the CPC aperture is relatively large. More incidence can enter the CPC, and the averaged heat flux on the absorber surface is larger. For example, when the concentration ratio is 8 and the incidence is vertical, the averaged heat flux on the absorber surface can reach 7.61 kW m^{-2}, while that for a fixed CPC is only 5.59 kW m^{-2}. When the incident angle is larger than the HAA_{max}, for a fixed CPC, the heat flux on the absorber surface decreases rapidly to 0 kW m^{-2} while that for a tracking CPC can still be maintained at a large magnitude. On the summer solstice in Beijing (φ = 40°), the solar elevation angle can be larger than 70°. The CPC with a concentration ratio of 8 has a HAA_{max} of 7.18° only. Correspondingly, the working hours for the non-tracking CPC is limited while the tracking CPC can break this limitation. In tracking mode, the CPC with a concentration ratio of 8 still has an averages heat flux of 5.02 kW m^{-2} at an incident angle of 35°. In this way, high collection temperature can be achieved over a day with a smaller collector area.

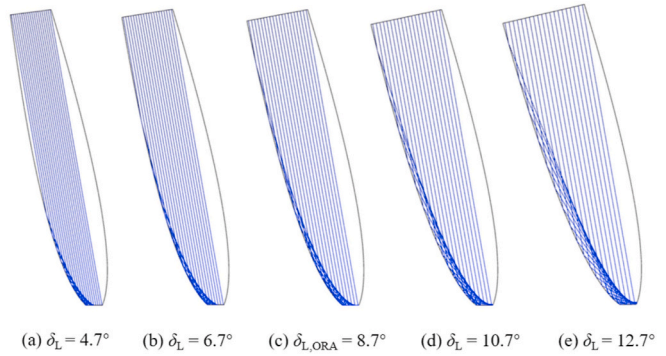

Fig. 16. Schematics of ray tracing under different rotation angles for CPC-L (C = 8, θ = 10°).

5.5. Effect of tracking error on concentration performance of CPC

TCPCMSC can concentrate incidence with an incident angle larger than the HAA_{max}, but the optical efficiency would be affected by tracking error as the common problem to conventional single or biaxial tracking systems. Fig. 18 shows the influence of the tracking error of CPC-R on the averaged heat flux on the absorber surface at different concentration ratios. It can be seen that when the tracking error is 0° and the CPC is rotated by the ORA, the averaged heat flux on the absorber surface reaches its largest magnitude. From this point, increasing or decreasing the rotation angle of CPC reduces the averaged heat flux on the absorber surface though increasing the rotation angle reduces the averaged heat flux at a smaller slope. Therefore, in operation practice, over-rotation of CPC-R is more conducive to reduce the reduction of heat

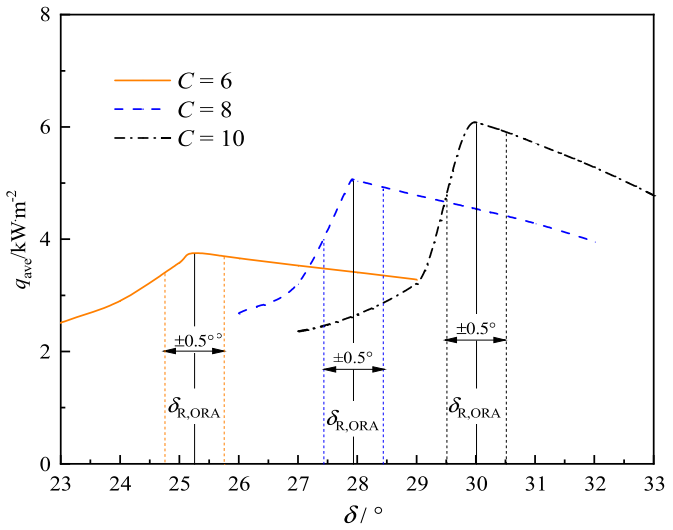

Fig. 18. Effect of tracking error on collection performance of CPC-R ($\theta = 35°$).

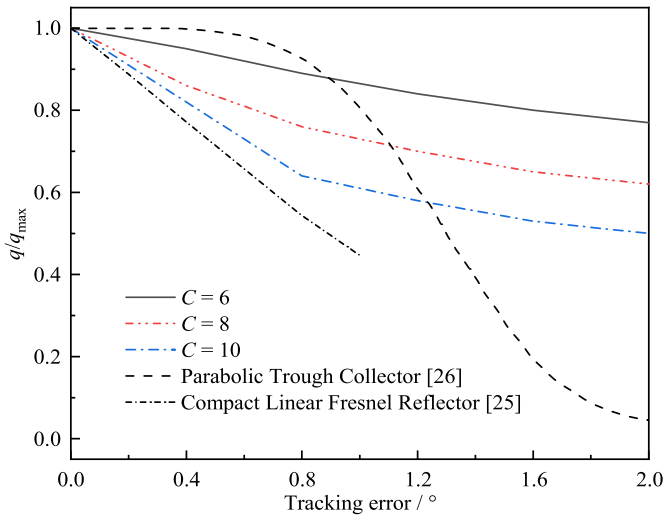

Fig. 19. Effect of tracking error on normalized optical efficiency ($\theta = 35°$).

flux caused by tracking error.

To obtain the maximum optical efficiency, the CPC needs to be rotated by the ORA during tracking. Larger deviation from the ORA (tracking error) results in lower optical efficiency. The normalized optical efficiency of TCPCMSC under different tracking errors is defined by Eq. (15) [25]:

$$\xi_n = \frac{\xi}{\xi_0} \tag{15}$$

Where ξ_0 is the optical efficiency when the tracking error is 0°.

As shown in Fig. 19, ξ_n of TCPCMSC decreases with the increase of tracking error, and the decreasing rate of ξ_n decreases. The ξ_n of compact linear fresnel reflector [25] is always lower than the ξ_n of TCPCMSC when the tracking error is in the range of 0–1°. As the tracking error increases, the ξ_n value of TCPCMSC decreases earlier than the ξ_n of PTC [26] when the tracking error is small. However, TCPCMSC has obvious advantages when the tracking error is large. With the increase of tracking error, the ξ_n of PTC decreases sharply to 0 while TCPCMSC can still maintain high concentration performance. When the concentration ratio is 10 and tracking error is 2°, the value of ξ_n can still reach 0.5 for TCPCMSC. The improvement on the accuracy of solar tracking system normally requires higher precision instruments, which would increase the initial cost of solar collectors [27]. In the present work, the relatedly lower tracking accuracy required lowers down the initial cost. In addition, the automatic tracking can largely bring the operating cost down. TCPCMSC can be used as an alternative which can achieve a relatively good collector performance at a low cost of investment by reducing the accuracy of the tracking system. In addition, unlike conventional tracking systems, tracking system of TCPCMSC is embodied in the collector, reducing the requirement on maintenance.

6. Conclusions

The concentration performances of a new TCPCMSC has been theoretical studied. To improve the collector efficiency, both reflective surfaces of CPC are independently rotated with the solar incidence angle. The ORA for each reflective surface of CPC under different incident angles is calculated. Ray-tracing simulation is carried out to analyze the heat flux distribution on the absorber surface under different working conditions. The following conclusions can be drawn:

(1) TCPCMSC can maintain high normalized optical efficiency even with large tracking errors, which helps to reduce the cost of solar collector.
(2) For the CPC of high concentration ratio, the tracking mode can help to break the limit of HAA_{max}. TCPCMSC can make full use of the solar radiation all over the daytime. Compared with non-tracking CPC, TCPCMSC can obtain a higher concentration ratio when the solar incidence angle is 0°. The maximum averaged heat flux on the absorber surface of a TCPCMSC of a concentration ratio 10 can reach 9.34 kW m^{-2}.
(3) When the rotation angle is smaller than the ORA, as rotation angle decreases, the averaged heat flux on the absorber surface decreases at a higher slope. When the rotation angle is larger than the ORA, as the rotation angle increases, the slope of the decrease in averaged heat flux is small. In operation practice, over-rotation of CPC-R is more conducive to reduce the reduction of heat flux caused by tracking error.
(4) The ORA of TCPCMSC is only related to time, latitude, collector inclination angle and CPC geometry.

CRediT authorship contribution statement

Rongji Xu: Conceptualization, Methodology, Data curation, Writing – review & editing. **Zhencheng He:** Software, Formal analysis, Data curation, Writing – original draft. **Liwei Yang:** Writing – review & editing, Visualization. **Shuhui Xu:** Formal analysis, Validation. **Ruixiang Wang:** Conceptualization. **Huasheng Wang:** Writing – review & editing.

Declaration of competing interest

The authors declare that they have no known competing financial interests or personal relationships that could have appeared to influence the work reported in this paper.

Data availability

No data was used for the research described in the article.

Acknowledgments

The present work was supported by the National Key R&D Program of China (No. 2020YFF0303904), National Natural Science Foundation of China (51506004), Beijing Municipal Natural Science Foundation

(3162009), BUCEA Post Graduate Innovation Project (PG2022059) and the Joint PhD Studentship of China Scholarship Council (CSC) and Queen Mary University of London (201808060459).

Nomenclature

a	aperture of CPC, m
C	concentration ratio
C_t	CPC truncation residual ratio
H_0	height of CPC, m
H	height of CPC (after truncation), m
n	days in a year
O	starting point of CPC-R
R	ending point of CPC-R
R′	ending point of CPC-R (after rotation)
s	width of microchannel absorber, m
T	time in 24 h
α	solar elevation angle, °
β	collector dip angle, °
γ	angle between the tangent to the starting point and the bottom (after rotation), °
δ	rotation angle, °
δ_R	rotation angle of CPC-R, °
δ_L	rotation angle of CPC-L, °
$\delta_{R,ORA}$	optimal rotation angle of CPC-R, °
$\delta_{L,ORA}$	optimal rotation angle of CPC-L, °
ε	angle between the OR and the bottom, °
η	angle between the tangent to the starting point and the bottom (before rotation), °
θ	solar incidence angle, °
θ_{max}	maximum half acceptance angle of CPC, °
λ	angle between the tangent to the ending point and vertical direction (before rotation), °
λ'	angle between the tangent to the ending point and vertical direction (after rotation), °
ξ	optical efficiency
ξ_n	normalized optical efficiency
σ	declination angle, °
φ	latitude, °
ω	angle between the tangent to the ending point and the bottom, °

Abbreviation

CPC	compound parabolic concentrator
CPC-L	left reflective surface of compound parabolic concentrator
CPC-R	right reflective surface of compound parabolic concentrator
HAA	half acceptance angle
ORA	optimal rotation angle
PTC	parabolic trough collector
TCPCMSC	tracking compound parabolic concentrator -microchannel tube solar collector

Appendix I. Derivation of optimal rotation angle of CPC-R ($\theta > \theta_{max}$)

As shown in Fig. 6(a), when the incident angle is larger than the HAA_{max}, the CPC-R rotates counterclockwise around the starting point O from OR to OR'.

At point R′, the angle of reflection equals the incident angle:

$$\theta - \lambda' = \angle PR'h' + \lambda' \tag{I-1}$$

In the △PR′h′ :

$$\angle PR'h' = \arctan\left(\frac{Ph'}{R'h'}\right) \tag{I-2}$$

Where the length of Ph' and R'h' are calculated by equations (I-3) and (I-4) respectively :

$$Ph' = PO + h'O = s + OR' \cdot \cos(\angle R'Oh) \tag{I-3}$$

$$R'h' = OR' \cdot \sin(\angle R'Oh) \tag{I-4}$$

Where OR' and ∠R'Oh are calculated by equations (I-5) and (I-6) respectively :

$$OR = OR^{'} = \frac{H}{\sin \varepsilon} \tag{I-5}$$

$$\angle R^{'} Oh = \varepsilon + \delta_{\mathrm{R,ORA}} \tag{I-6}$$

In this case, equations (I-1) can be expressed as:

$$\theta = \arctan\left(\frac{s + \frac{H}{\sin \varepsilon}\cdot\cos\left(\varepsilon + \delta_{\mathrm{R,ORA}}\right)}{\frac{H}{\sin \varepsilon}\cdot\sin\left(\varepsilon + \delta_{\mathrm{R,ORA}}\right)}\right) + 2\lambda^{'} \tag{I-7}$$

Where ε stand for the angle between OR and the absorber; λ' stand for the angle between the tangent line of CPC at point R′ and the vertical direction.

The ε can be calculated from equations (I-8) to equations (I-12), in △ORh:

$$\tan \varepsilon = \frac{H}{Oh} = \frac{H}{Ph - s} \tag{1–8}$$

Where Ph can be expressed as:

$$Ph = H\cdot\tan(\angle PRh) \tag{1–9}$$

The ∠PRh at point R can be expressed as:

$$\angle PRh = \theta_{\max} + 180^{\circ} - 2\omega \tag{1–10}$$

Where ω is the angle between the tangent line of the ending point and the absorber.

Therefore, ε can be expressed as equation (I-11):

$$\varepsilon = \arctan\left(\frac{H}{H\cdot\tan(\theta_{\max} + 180^{\circ} - 2\omega) - s}\right) \tag{I-11}$$

Where λ' can be calculated by equations (I-12):

$$\lambda^{'} = \delta_{\mathrm{R,ORA}} - \lambda = \delta_{\mathrm{R,ORA}} - (90 - \omega) \tag{1–12}$$

Based on equation (I-2)-(I-12), equation (I-1) can be expressed as :

$$\theta = \arctan\left\{\frac{s + \frac{H\cdot\cos\left[\arctan\left(\frac{H}{H\cdot\tan(\theta_{\max}+180^{\circ}-2\omega)-s}\right)+\delta_{\mathrm{R,ORA}}\right]}{\sin\left[\arctan\left(\frac{H}{H\cdot\tan(\theta_{\max}+180^{\circ}-2\omega)-s}\right)\right]}}{\frac{H\cdot\sin\left[\arctan\left(\frac{H}{H\cdot\tan(\theta_{\max}+180^{\circ}-2\omega)-s}\right)+\delta_{\mathrm{R,ORA}}\right]}{\sin\left[\arctan\left(\frac{H}{H\cdot\tan(\theta_{\max}+180^{\circ}-2\omega)-s}\right)\right]}}\right\} + 2\left(\delta_{\mathrm{R,ORA}} + \omega\right) - 180^{\circ} \tag{I-13}$$

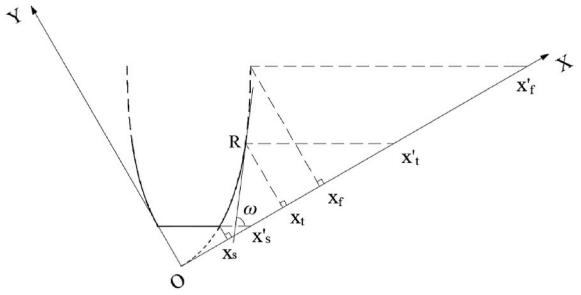

Fig. 20. Schematic of terminal coordinates with different truncation ratios

Where ω can be calculated from equations (I-14) to equations (I-18). As shown in Fig. 20, lines parallel to the heat absorber through the starting and ending points of CPC-R intersect the X-axis at points x′s and x′f respectively. The abscissa of the points are obtained by equations (I-14) and (I-15) :

$$x_{\mathrm{s}}^{'} = \frac{s(1 + \sin \theta_{\max})}{2 \tan \theta_{\max}} \tag{I-14}$$

$$x_{\mathrm{f}}^{'} = \frac{2(s + a)\sin \theta_{\max} + s(1 - \sin \theta_{\max})\left(1 + \frac{1}{\sin \theta_{\max}}\right)^{2}}{2 \tan \theta_{\max}} \tag{I-15}$$

The interval between points x’s and x’f on the X-axis corresponds to the truncation ratio of CPC in the range 0–1. The abscissa of x’t corresponds to

the desired truncation ratio and can be obtained according to equation (I-16):

$$x_t^{'} = x_s^{'} + C_t\left(x_f^{'} - x_s^{'}\right) \tag{I-16}$$

For a line parallel to the absorber through the x'$_t$, the intersection of this line with CPC-R can be found by equation (I-17):

$$\begin{cases} g = -\tan\theta_{max}\left(x - x_t^{'}\right) \\ y = \dfrac{x^2}{2s(1+\sin\theta_{max})} \end{cases} \quad (x>0) \tag{I-17}$$

The ending point of CPC-R after truncation, the point R, can be obtained at (x_t, y_t). The angle between the tangent line at point R of CPC-R and the heat absorber can be obtained as :

$$\omega = \arctan[y^{'}(x_t)] + \theta_{max} \tag{I-18}$$

According to equations (I-16)-(I-20), the value of ω is a constant derived according to the geometry parameters of CPC including concentration ratio C, truncation ratio C_t, width of absorber s and aperture width a.

Appendix II. Derivation of optimal rotation angle of CPC-R ($\theta < \theta_{max}$)

As shown in Fig. 6(b), when CPC-R rotates clockwise around point O, the rotation angle is the angle between the tangent lines at the starting points before and after rotation.

When CPC-R rotates by the ORA, the incident ray goes to point O, and is then reflected to point P. At point O, the following relation can be obtained:

$$\gamma = \gamma_1 = \gamma_2 \tag{II-1}$$

$$\theta + 90^{\circ} = 2\gamma \tag{II-2}$$

$$\gamma = \eta - \delta_{R,ORA} \tag{II-3}$$

Therefore, the relation between the ORA and incident angle can be expressed as (II-4):

$$\delta_{R,ORA} = \eta - \frac{90^{\circ} + \theta}{2} \tag{II-4}$$

Appendix III. Derivation of optimal rotation angle of CPC-L

As shown in Fig. 7(a), when $\theta > 0°$, the CPC-L rotates counterclockwise around the starting point P. When the incident angle is relatively large, the CPC-L rotates to the position where it cannot work. The lines connecting the starting and ending points of CPC-L are parallel to the incidence. As expressed in equation (III-1) :

$$\delta_{L,ORA} = \varepsilon + \theta - 90^{\circ} \tag{III-1}$$

As the incident angle decreases, the CPC-L can work to concentrate incidence. As shown in Fig. 7(b), the rotation angle is the angle between the tangent lines at the starting points before and after rotation. When CPC-L rotates by the ORA, the incidence can be reflected to point O through point P. At point P, there are:

$$90^{\circ} - \theta = 2\gamma \tag{III-2}$$

$$\delta_{L,ORA} = \eta - \gamma \tag{III-3}$$

In this case, the ORA of CPC-L is expressed by equation (III-4) :

$$\delta_{L,ORA} = \eta - \frac{90^{\circ} - \theta}{2} \tag{III-4}$$

According to equations (III-1) and (III-4), for the CPC-L, the ORA can be given by equation (III-5) :

$$\delta_{L,ORA} = \max\begin{cases} \eta - \dfrac{90^{\circ} - \theta}{2} \\ \varepsilon + \theta - 90^{\circ} \end{cases} \tag{III-5}$$

References

[1] Laveet Kummar, M. Hasanuzzaman, N.A. Rahim, Global advancement of solar thermal energy technologies for industrial process heat and its future prospects: a review, Energy Convers. Manag. 195 (2019) 885–908.

[2] Shiva Gorjian, Hossein Ebadi, Francesco Calise, Ashish Shukla, Carlo Ingrao, A review on recent advancements in performance enhancement techniques for low-temperature solar collectors, Energy Convers. Manag. 222 (2020), 113246.

[3] Winston Roland, Principles of solar concentrators of a novel design, Sol. Energy 16 (1974) 89–95.

[4] Rongji Xu, Yuanqiang Zhao, Hao Chen, Qingping Wu, Liwei Yang, Huasheng Wang, Numerical and experimental investigation of a compound parabolic concentrator-capillary tube solar collector, Energy Convers. Manag. 204 (2020), 112218.

[5] Ahed Hameed Jaaz, Husam Abdulrasool Hasan, Kamaruzzaman Sopian, Mohd Hafidz Bin, Haji Ruslan, Saleem Hussain Zaidi, Design and development of compound parabolic concentrating for photovoltaic solar collector: Review, Renew. Sustain. Energy Rev. 76 (2017) 1108–1121.

[6] Rongji Xu, Xiaohui Zhang, Ruixiang Wang, Shuhui Xu, Huasheng Wang, Experimental investigation of a solar collector integrated with a pulsating heat pipe and a compound parabolic concentrator, Energy Convers. Manag. 148 (2017) 68–77.
[7] Runsheng Tang, Maogang Wu, Yamei Yu, Li Ming, Optical performance of fixed east–west aligned CPCs used in China, Renew. Energy 35 (2010) 1837–1841.
[8] Chen Lin, Jiaxiang Chen, Xinrong Zhang, Numerical simulation on the optical and thermal performance of a modified integrated compound parabolic solar concentrator, Int. J. Energy Res. 13 (2015).
[9] Yinfeng Wang, Haijun Chen, Xin Zhang, Lizhu Jin, Tingting Ma, Yuezhao Zhu, Optical and thermal performance of sun-tracking cpc heat pipe evacuated tubular collector, Acta Energiae Solaris Sin. 36 (11) (2015) 2643–2650.
[10] Sainath A. Waghmare, Kaustubh V. Chavan, Nitin P. Gulhane, Numerical simulation of tracking modes for compound parabolic collector with tubular receiver, IEEE International Conference on Power Electronics 55 (2) (2018) 1882–1889.
[11] O. Achkari, A. El Fadar, I. Amlal, A. Haddi, M. Hamidoum, S. Hamdoune, A new sun-tracking approach for energy saving, Renew. Energy 169 (2021) 820–835.
[12] Ahmadreza Yazdanbakhsh, Reza Nemati, Mohamadreza Massoudinejad, Mohanadjavad Jafari, Masoomeh Dashtdar, Solar photodegradation of carbamazepine from aqueous solutions using a compound parabolic concentrator equipped with a sun tracking system, Open Chem 17 (2019) 477–484.
[13] Ya-ling He, Kun Wang, Du Bao-cun, Yu Qiu, Zhangjing Zheng, Liang Qi, Non-uniform characteristics of solar flux distribution in the concentrating solar power systems and its corresponding solutions: a review, Chin. Sci. Bull. 61 (30) (2020) 3208–3237.
[14] Sumon Dey Chandana, Sujan Kumara Paidisetty, K.S. Reddyd, Bala Pesala, Optical and electrical performance investigation of truncated 3X non-imaging low concentrating photovoltaic-thermal systems, Energy Convers. Manag. 220 (2020), 113056.
[15] Rongji Xu, Yusen Ma, Meiyu Yan, Chao Zhang, Shuhui Xu, Ruixiang Wang, Effects of deformation of cylindrical compound parabolic concentrator(CPC) on concentration characteristics, Sol. Energy 176 (2018) 73–86.
[16] Jintao Xu, Chen Fei, Chengang Deng, Design and analysis of a novel multi-sectioned compound parabolic concentrator with multi-objective genetic algorithm, Energy 225 (2021), 120216.
[17] Chai Lei, Rabia Shaukat, Liang Wang, Huasheng Wang, A review on heat transfer and hydrodynamic characteristics of nano/microencapsulated phase change slurry (N/MPCS) in mini/microchannel heat sinks, Appl. Therm. Eng. 135 (2018) 334–349.
[18] Xinyu You, Jionghui Liu, Hua Nan, Jing Wang, Rongji Xu, Guangxu Yu, Experimental study on flow boiling of refrigerant R1233zd(E) in microchannels: heat transfer, Appl. Therm. Eng. 180 (2021), 116083.
[19] Mathew Georgea, A.K. Pandeyb, Nasrudin Abd Rahima, V.V. Tyagic, Shahabuddinb Syed, R. Saidur, Concentrated photovoltaic thermal systems: a component-by-component view on the developments in the design, heat transfer medium and applications, Energy Convers. Manag. 186 (2019) 15–41.
[20] Zhangyuan Wang, Zicong Huang, Fucheng Chen, Xudong Zhao, Peng Guo, Experimental investigation of the novel BIPV/T system employing micro-channel flat-plate heat pipes, Build. Serv. Eng. (2018) 1–17, 0.
[21] Ari Rabl, Optical and thermal properties of compound parabolic concentrators, Sol. Energy 18 (1976) 497–511.
[22] Faisal Masood, Perumal Nallagownden, Irraivan Elamvazuthi, Javed Akhter, Mahammad Azad Alam, A new approach for design optimization and parametric analysis of symmetric compound parabolic concentrator for photovoltaic applications, Sustainability 13 (2021) 4606.
[23] Abid Ustaoglu, Junnosuke Okajima, Xinrong Zhang, Shigenao Maruyama, Truncation effects in an evacuated compound parabolic and involute concentrator with experimental and analytical investigations, Appl. Therm. Eng. 138 (2018) 433–445.
[24] M. Smyth, A. Zacharopoulos, P.C. Eames, B. Norton, An experimental procedure to determine solar energy flux distributions on the absorber of line-axis compound parabolic concentrators, Renew. Energy 16 (1/4) (1999) 761–764.
[25] Gang Wang, Shen Fan, Fasi Wang, Zeshao Chen, Design and experimental study of a solar CPV system using CLFR concentrator, Sustain. Energy Technol. Assessments 40 (2020), 100751.
[26] Fabienne Sallaberry, Ramon Pujiol-Nadal, Marco Larcher, Mercedes Hannelore, Rittmann Frank, Direct tracking error characterization on a single-axis solar tracker, Energy Convers. Manag. 105 (2015) 1281–1290.
[27] Nsengiyumva Walter, Shiguo Chen, Lihua Hu, Xueyong Chen, Recent advancements and challenges in solar tracking systems (STS): a review, Renew. Sustain. Energy Rev. 81 (2018) 250–279.